AGU PUBLICATIONS

JGR

Journal of Geophysical Research: Space Physics

RESEARCH ARTICLE

10.1002/2016JA022671

Key Points:
- Progress in studying the ionosphere irregularities in the equatorial electrojet
- Energy conservation in a fluid model of plasma instabilities
- Verifing the theory of forward and reverse energy cascading in the equatorial electrojet

Correspondence to:
E. Hassan,
ehab@utexas.edu

Citation:
Hassan, E., D. R. Hatch, P. J. Morrison, and W. Horton (2016), Multiscale equatorial electrojet turbulence: Energy conservation, coupling, and cascades in a baseline 2-D fluid model, *J. Geophys. Res. Space Physics*, *121*, 9127–9145, doi:10.1002/2016JA022671.

Received 8 MAR 2016
Accepted 30 AUG 2016
Accepted article online 6 SEP 2016
Published online 22 SEP 2016

Multiscale equatorial electrojet turbulence: Energy conservation, coupling, and cascades in a baseline 2-D fluid model

Ehab Hassan[1,2], D. R. Hatch[3], P. J. Morrison[3], and W. Horton[3,4]

[1]ICES, University of Texas at Austin, Austin, Texas, USA, [2]Department of Physics, Ain Shams University, Cairo, Egypt, [3]IFS, University of Texas at Austin, Austin, Texas, USA, [4]ARL, University of Texas at Austin, Austin, Texas, USA

Abstract Progress in understanding the coupling between plasma instabilities in the equatorial electrojet based on a unified fluid model is reported. Simulations with parameters set to various ionospheric background conditions revealed properties of the gradient-drift and Farley-Buneman instabilities. Notably, sharper density gradients increase linear growth rates at all scales, whereas variations in cross-field $\boldsymbol{E} \times \boldsymbol{B}$ drift velocity only affect small-scale instabilities. A formalism defining turbulent fluctuation energy for the system is introduced, and the turbulence is analyzed within this framework. This exercise serves as a useful verification test of the numerical simulations and also elucidates the physics underlying the ionospheric turbulence. Various physical mechanisms involved in the energetics are categorized as sources, sinks, nonlinear transfer, and cross-field coupling. The physics of the nonlinear transfer terms is studied to identify their roles in producing energy cascades, which explain the generation of small-scale structures that are stable in the linear regime. The theory of two-step energy cascading to generate the 3 m plasma irregularities in the equatorial electrojet is verified for the first time in the fluid regime. In addition, the nonlinearity of the system allows the possibility of an inverse energy cascade, potentially responsible for generating large-scale plasma structures at the top of the electrojet as found in different rocket and radar observations.

1. Introduction

The mixing of turbulent structures of different scale lengths is important for understanding plasma turbulence driven by instabilities in the ionosphere. In the equatorial electrojet, Farley-Buneman and gradient-drift instabilities are driven by a large eastward electrojet current and an $\boldsymbol{E} \times \boldsymbol{B}$ drift due to an electron density gradient, respectively [*Farley*, 2009]. Echoes of Farley-Buneman instability are called "Type I" because they were the first observed using the coherent backscattering radar at Jicamarca by *Bowles et al.* [1963]. However, echoes for gradient-drift instability are observed only during the absence of the Type I instability (when the electron drift speed is less than the local ion-acoustic speed, C_s) and are called "Type II" [*Balsley*, 1969; *Fejer et al.*, 1975]. A unified fluid model that describes both types of plasma instabilities in the equatorial electrojet under various solar conditions was discussed by *Hassan et al.* [2015]. Simulation results of this unified fluid model elucidated some facets of the nature of the coexistence and coupling between Farley-Buneman and gradient-drift instabilities in both the linear and nonlinear regimes. The present work is a continuation of this previous study.

In situ measurements taken by a sounding rocket launched from Lobos, Peru, during CONDOR campaign revealed electrostatic characteristics of the *E* region instabilities [*Pfaff et al.*, 1987a]. These measurements also showed maximum variations of the spectral energy at frequencies less than 100 Hz at 90–103 km altitudes which extends to higher frequencies (~1000 Hz) at 103–108 km altitudes. Simultaneously, a backscattering radar measurement taken at Jicamarca, Peru, showed a strong Type I echo of 3 m wavelength which is modified by long-scale horizontally propagating Type II waves [*Kudeki et al.*, 1987]. In *Hassan et al.* [2013, 2015] the linear growth-rate profile in the vertical direction of the ionosphere was seen to have three distinct regions in the equatorial electrojet: The lower region (90–103 km) being dominated by the gradient-drift instability, the higher region (108–115 km) being dominated by the Farley-Buneman instability, and the middle region (103–108) showing a strong coupling between the two types of plasma instabilities. Under varying ionospheric conditions, linear and nonlinear simulation results that reproduce many of the radar and rocket

observations were described in that paper and light was shed on the physical mechanisms that drive these instabilities and are responsible for the coupling between them. The rocket measurements during *Guará* Campaign show the magnitude of the vertical DC electric field to be 10–15 mV/m at 105 km, which corresponds to a zonal cross-field drift in the range 400–500 m/s (where $B_o \simeq 2.5$ G) [*Pfaff et al.*, 1997]. This zonal drift speed exceeds the local ion-acoustic speed within the equatorial electrojet in the daytime where $C_s = 318.5$ m/s, and the Farley-Buneman instability can be easily driven around the *E* region peak. Due to the high computational cost of simulating the unified fluid model, we choose to simulate two cases for which the cross-field drift is 400 and 425 m/s, respectively.

The electric field in the equatorial electrojet region was observed by *Hysell and Burcham* [2000] using JULIA radar at the Jicamarca observatory. The observation measurements indicate that the peak of the electrojet electric field is at 105 km altitude. The small plasma structures ($\lesssim$10 m) were found to have the largest drift speed of magnitudes greater than 400 m/s compared to irregularities of larger sizes. The observations of another campaign which was held in Jicamarca on 26 July 2005 were reported by *Hysell et al.* [2007]. They used five different radar diagnostic systems to give detailed characteristics of the plasma instabilities in the equatorial electrojet. The spatially variable polarization electric field was found to have its strongest magnitude close to the cutoff altitude of the gradient-drift instability at the *E* region peak ($\simeq$105 km). In addition, *Hysell et al.* [2007] reported the dominance of the 3 m plasma structure in the spectra due to their strong echoes. Moreover, the Doppler shift of Type I irregularities supports the previous observations by *Pfaff et al.* [1987a, 1987b], *Kudeki et al.* [1987], and *Hysell and Burcham* [2000] about the limit of small structure drifts to the ion-acoustic speed (C_s). The simulation results of the unified fluid model presented in the previous work [*Hassan et al.*, 2015 and *Hassan*, 2016] and the present work show a very good agreement with these radar measurements.

Theoretically, *Sudan et al.* [1973] proposed a two-step energy cascading mechanism to explain the generation of small structures in the electrojet caused by the Farley-Buneman instability. The energy in the large structures of kilometer scale length, which are excited in the electrojet by the gradient-drift instability for a positive density gradient, is cascaded to the intermediate-scale waves that have wavelength of tens of meters. These intermediate irregularities, in turn, cascade their energy into the short-scale waves of 1–3 m scale length. This transference can take place when there is a large horizontal density gradient compared to the background vertical gradient and in addition can be induced by the increase of the vertically perturbed plasma drifts to an order of magnitude above the horizontal electron drift [*Farley and Balsley*, 1973]. The nonlinear simulation results that we present in this present paper show a redistribution of energy from the large structures to the small ones in the vertical direction, which verifies the two-step energy cascading mechanism proposed by *Sudan et al.* [1973].

Nonlinear coupling between two unstable modes propagating in nearly the same direction can give rise to a forward cascading of energy from large structures to the short ones. However, the nonlinear interaction between two unstable waves of short wavelength might cause an inversem cascade of energy to generate a stable large-scale structure. The nonlinear coupling mechanisms between the linearly unstable modes were also found to be sensitive to the aspect angle of the equatorial irregularities [*Kudeki and Farley*, 1989 and *Lu et al.*, 2008]. Studying the energy cascading in our unified fluid dynamical system shows the ability of the gradient-drift instability to generate small-scale instability of the order of a meter and less in a forward energy cascading process. There also exists, via a separate nonlinear mechanism, a smaller nonlinear transfer channel whereby the Farley-Buneman instability transfers energy from the submeter structures to irregularities of tens of meters scale size through a reverse energy cascading mechanism.

Our paper is organized as follows. In section 2 we present the unified fluid model equations, including some linear and nonlinear numerical results in sections 2.1 and 2.2, respectively. Next, in section 3, we present the energy equation for the evolving fields. Here we separate out terms that correspond to sources, sinks, nonlinear transfer, and coupling. Then, in section 3.1, we examine the total energy content and its temporal variations in our simulations, followed in section 3.2, by an investigation of the roles of sources and sinks of energy in the system. This is followed up in section 4 where the transfer of energy, cascading, among the unstable modes is investigated. Finally, in section 5 we summarize our findings.

2. Unified Fluid Model

As noted above, in the previous work of *Hassan et al.* [2015] the 2-D unified fluid model that unifies the Farley-Buneman and gradient-drift instabilities was derived. There it was shown that this model has linear

results that are comparable to the kinetic treatment of the Farley-Buneman plasma instability by *Schmidt and Gary* [1973], and simulation results also showed good agreement with the radar measurements and sounding rocket observations. The unified fluid model is composed of the following set of nonlinear partial differential equations that control the plasma dynamics and energy coupling between the unstable modes:

$$\partial_t n = \boldsymbol{\nabla} \cdot (n \boldsymbol{\nabla} \chi) \tag{1}$$

$$\partial_t \chi = \upsilon_{t_i}^2 \ln(n) + \frac{\Omega_{ci}}{B}\phi - \nu_{in}\chi + \frac{1}{2}|\boldsymbol{\nabla}\chi|^2 + \frac{4}{3}\frac{\upsilon_{t_i}^2}{\nu_{in}}\nabla^2\chi \tag{2}$$

$$\begin{aligned}\partial_t \nabla^2\phi = {} & \frac{T_e \nu_{en}}{e}\nabla^2 \ln(n) - \nu_{en}\nabla^2\phi - B\Omega_{ce}\nabla^2\chi - \Omega_{ce}\left[\phi, \ln(n)\right] - \frac{1}{B}\left[\phi, \nabla^2\phi\right] \\ & + \frac{T_e \nu_{en}}{e}\boldsymbol{\nabla}\ln(n)\cdot\boldsymbol{\nabla}\ln(n) - \nu_{en}\boldsymbol{\nabla}\ln(n)\cdot\boldsymbol{\nabla} - B\Omega_{ce}\boldsymbol{\nabla}\ln(n)\cdot\boldsymbol{\nabla}\chi,\end{aligned} \tag{3}$$

where υ_{t_i} (225.2 m/s) is the ion thermal speed, ν_{in} (3.2×10^3 s^{-1}) and ν_{en} (2.3×10^4 s^{-1}) are, respectively, the ion and electron collision frequencies with the background neutrals, Ω_{ci} (1.13×10^2 s^{-1}) and Ω_{ce} (6.5×10^6 s^{-1}) are the ion and electron gyration frequencies, T_e (192.1 K) is the isothermal temperature of ions and electrons, B (3.7×10^{-5} T) is the background magnetic field, and $\left[f, g\right]$ is the Jacobian (Poisson) bracket which is defined as $[f, g] = \partial_x f \partial_y g - \partial_x g \partial_y f$.

The three dynamical variables of the unified fluid model are n, χ, and ϕ. Specific details regarding the justification for this model are given in *Hassan et al.* [2015]; here we note two key ingredients. The variable n is the plasma density of either species, since quasineutrality has been assumed. Because of the large ratio between the ion collision frequency with the neutral particles and the ion gyration frequency [*Kelley*, 2009], the ions are considered unmagnetized and the following approximation for the ion fluid velocity was assumed:

$$\boldsymbol{\upsilon}_i = -\boldsymbol{\nabla}\chi.$$

Because of the small temporal and spatial variations in the background magnetic field during the solar quiet times [*Farley*, 2009] and because of the electrostatic nature of the plasma waves in the equatorial electrojet, the **E** field was assumed to be of the form

$$\mathbf{E} = -\boldsymbol{\nabla}\phi.$$

The linear and nonlinear simulation results of this model reproduce many features that are found in the radar and rocket observations as we will show below. The 2-D simulation box is centered at 105 km altitude, and it extends over 100 m × 100 m in y and z directions. The grid size in the spectral domain is $\Delta k = \pi/16$ m^{-1} in both directions, and the spectral domains expand in the y and z directions up to $k_{y,max} = 21$ m^{-1} and $k_{z,max} = 2.1$ m^{-1}, respectively, to cover a whole range of possible wavelengths for the plasma fluctuations that can be generated in the equatorial electrojet.

The International Reference Ionosphere, Mass Spectrometer and Incoherent Scatter (MSIS) Radar, and International Geomagnetic Reference Field empirical models are employed to calculate the background parameters in the ionosphere (e.g., electron densities and ions compositions), the neutral atmosphere compositions, and the background magnetic field, respectively, under the solar maximum conditions on 21 March 1987 at noontime [*Hassan et al.*, 2015]. The ion-acoustic speed is roughly 318.5 m/s. However, the magnitude of the electric field components (E_y and E_z) and the density-gradient scale length (L_n) in the current work were set at specific values to probe their influence on the plasma turbulence and the saturation levels of the fluctuating plasma density and perturbed electric field.

2.1. Linear Results

Based on the radar observations of Type I and Type II instabilities in the equatorial electrojet, a standard fluid model was proposed by *Fejer et al.* [1975] that unifies Farley-Buneman and gradient-drift instabilities. The linear phase velocity (υ_{ph}) and growth rate (γ) in the standard fluid model are given by

$$\upsilon_{ph} = \frac{V_d}{1+\psi} \tag{4}$$

$$\gamma = \frac{1}{(1+\psi)^2}\left[\frac{k^2\psi}{(1+\psi)\nu_{in}}\left(V_d^2 - C_s^2\right) + \frac{V_d \nu_{in}}{L_n \Omega_{ci}}\right] \tag{5}$$

where V_d is the cross-field drift velocity, C_s is the ion-acoustic speed, and $\psi = \frac{\nu_{in}\nu en}{\Omega_{ci}\Omega_{ce}}$.

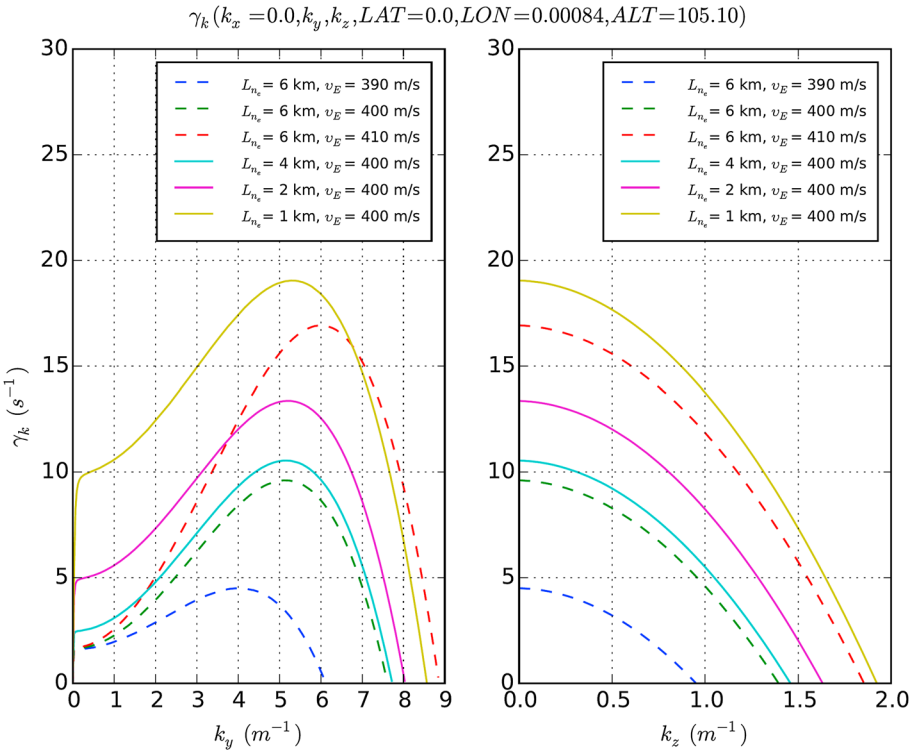

Figure 1. The dependence of the growth rates at 105 km altitude on the (left) horizontal (k_y)and (right) vertical (k_z) wave numbers is shown for different values of the electron density scale lengths L_n (top) and cross-field ($\boldsymbol{E} \times \boldsymbol{B}$) drifts.

The phase velocity in equation (4) according to the standard fluid model of the equatorial electrojet is always constant (at constant ψ) and equal to the cross-field drift velocity. That means the phase velocity could be greater than the ion-acoustic speed in cases where the background vertical DC electric field (~10–20 mV/m) is large at different regions of the ionosphere. This contradicts the radar observations that show that the phase velocity is limited to the ion-acoustic speed at those regions.

On the other hand, the growth rate in equation (5) shows two possibilities to make the plasma unstable. The first term on the right-hand side makes the dynamical system unstable when the cross-field drift speed (V_d) is greater than the ion-acoustic speed (C_s). This instability was studied by *Farley* [1963] and *Bunemann* [1963] in the fluid and kinetic regimes, respectively. When the cross-field drift velocity is smaller than the ion-acoustic speed, this instability disappears from the radar backscattering echoes. However, gradient-drift instability is driven in the equatorial electrojet due to the sharp gradient in the electron density between 100 and 115 km. The negative density gradient above 115 km precludes the generation of Type II instability [*Hassan*, 2016]. Although the ion-acoustic speed is a threshold for the generation of Type I unstable waves, no threshold can be found for Type II instabilities. This means that the Type II instability is always present in the electrojet, but it is hard to be detected in the presence of the Type I instability [*Farley and Balsley*, 1973; *Forbes*, 1981]. A disadvantage of the standard fluid model is the monotonic increase in the growth-rate profile as a function of the wave number with no evidence of any stabilization of the unstable modes. This limits the usability of the standard fluid model in studying the evolution of Farley-Buneman instability and its coupling with the gradient-drift instability.

In the unified fluid model we proposed in *Hassan et al.* [2014, 2015], the dynamical system described by equations (1)–(3) can be linearized by separating out the stationary background from the fluctuating part as $\tilde{n} = n_o + \delta\tilde{n}$, $\tilde{\phi} = \phi_o + \delta\tilde{\phi}$, and $\tilde{\chi} = \chi_o + \delta\tilde{\chi}$, where $\nabla\chi_o = 0$. Then we can solve the linearized equations numerically to find the eigenvalues and eigenvectors for our linear system, giving as usual the growth rate and frequency (and by extension, phase velocity) as the imaginary and real parts of the eigenvalues, respectively.

In Figure 1, the growth-rate profiles are shown as a function of k_y (left) and k_z (right). Choosing $k_{\min} = \pi/16\ \mathrm{m}^{-1}$ for both the horizontal and vertical directions gives rise to a single peak in $\gamma(k_z)$ and two peaks in $\gamma(k_y)$, with one located at small values of k_y. In Figure 1 (right), it is seen that there is no minimum or

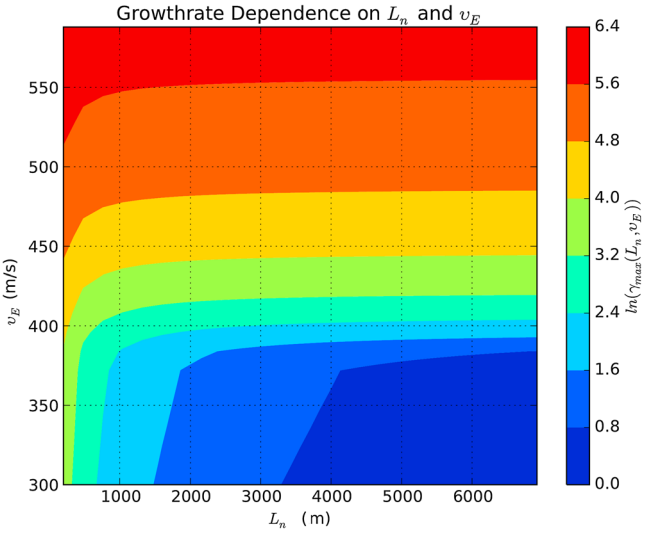

Figure 2. The dependence of the growth rates at 105 km altitude on the density-gradient scale-length L_n and the cross-field drift v_E. The large scale length does not have much effect on the growth rate; for example, above the ion-acoustic speed scale lengths greater than 2 km have no effect on the growth rate.

threshold wave number for exciting unstable modes and the peak in $\gamma(k_z)$ is found at $k_z = 0$. This means that unstable modes are always present in the vertical direction as a result of the electron $\boldsymbol{E} \times \boldsymbol{B}$ drift v_E and a positive density-gradient scale length L_n. However, examination of Figure 1 (left) reveals two peaks in the k_y-dependent growth rate. Observe a short peak at small k_y near $k_y = \pi/16$ m^{-1}, which manifests itself by generating plasma waves of long wavelength. The clear maximum of $\gamma(k_y)$ at larger k_y can be associated with the linear excitation of short-scale (submeter) plasma structures.

The electron density-gradient scale length and $\boldsymbol{E} \times \boldsymbol{B}$ drifts are the salient parameters in driving the plasma instabilities at small and large wave numbers. The solid lines in Figure 1 show the effect of different L_n (at a constant drift speed, $v = 400$ m/s) in driving the instabilities at small wave numbers for the $\gamma(k_y)$ and $\gamma(k_z)$ profiles. The short density-gradient scale length gives rise to a higher peak at the small wave numbers for the growth-rate profiles in the horizontal and vertical directions. In addition, this short L_n affects the height of the $\gamma(k_y)$ peak at large wave numbers. Therefore, the density-gradient scale length plays a very important role in driving equatorial electrojet instabilities for structures of different scale lengths.

On the other hand, the electron's $\boldsymbol{E} \times \boldsymbol{B}$ drift only affects the height of the growth-rate profile in the horizontal direction $\gamma(k_y)$ at the large wave numbers (small structures), where the drift velocity is observed to increase growth rates. In some other cases (not shown here) we have examined the growth rates when $\boldsymbol{E} \times \boldsymbol{B}$ drifts are smaller than the local ion-acoustic speed. In these cases, the peak at large wave numbers in the $\gamma(k_y)$ profile disappears, but the one at small wave numbers does not. Therefore, the instability at the large wave numbers is due to the two-stream instability that is excited when the relative speed between the electrons and ions exceeds the ion-acoustic speed. Also, there is no minimum threshold for the cross-field drift to excite the gradient-drift instability at the small wave numbers, although it has to be greater than zero.

Therefore, the growth-rate profiles at different magnitudes of the ionosphere background electric field and density gradient show a strong stabilization. This stabilization takes place at the effective scale length of the plasma irregularities generated as a result of the Farley-Buneman instability mechanism. In addition, the linear phase velocity profile, which is discussed in *Hassan et al.* [2015] and *Hassan* [2016], has its magnitude decreased below the cross-field drift speed and close to the local magnitude of the ion-acoustic speed in the equatorial electrojet. Hence, the unified fluid model in the linear regime was able to match the observations of the reduced phase velocity in the equatorial electrojet. Also, the strong stabilization of the linear growth rate around the effective wave numbers of the Farley-Buneman instability demonstrates the possibility of a saturation of the perturbed fields in the nonlinear regime.

Another representation of the variation of the growth rate with the density-gradient scale length L_n and the cross-field drift v_E is shown in Figure 2. Note the positive growth rate for all values of L_n and v_E which proves the presence of at least one type of instability (i.e., Type II) in the equatorial electrojet region even in the absence of Type I instability when the cross-field drift speed is less than the ion-acoustic speed. In the region below the ion-acoustic speed the growth rate of Type II instability is influenced by variations in the density-gradient scale-length L_n and the cross-field drift speed v_E. Below $L_n = 1.5$ km, the scale length dominates and the change in the growth rate due to the cross-field drift is negligible. In contrast, above $L_n = 4.0$ km, the variation in growth rate due to the change in the density-gradient scale length is very small compared to the effect of

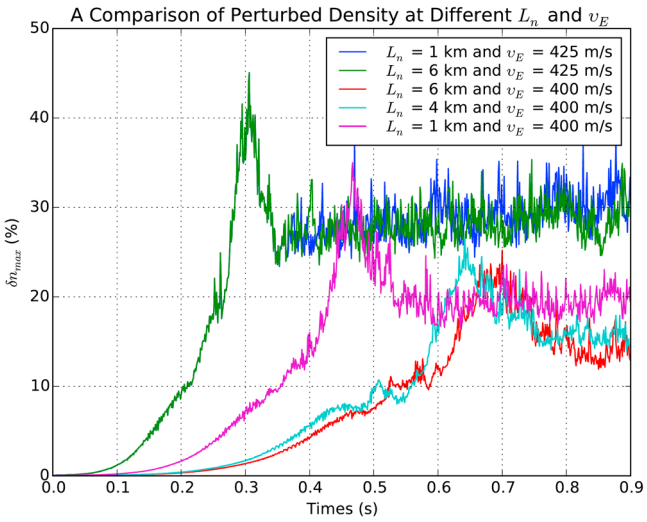

Figure 3. A comparison between perturbed density maxima for different density-gradient scale lengths, $L_n = 1$, 4, and 6 (km) and cross-field ($\boldsymbol{E} \times \boldsymbol{B}$) drifts, $v_E = 400$ and 425 (m/s).

the variation of the cross-field drift on the growth rate. In the transition region ($L_n = 1.5$–4.5 km), the variation in the growth rate is influenced by the variations in L_n and v_E. Thus, the plasma dynamics of Type II instability in the equatorial electrojet depends on the background parameters in the three ranges indicated above.

In the presence of Type I instability, when the cross-field drift exceeds the ion-acoustic speed, the effect of v_E dominates the instability growth rate and the variations in the density-gradient scale length plays a negligible role in evolving the unstable modes especially in the range above 1 km. Moreover, for large values of electron $\boldsymbol{E} \times \boldsymbol{B}$ drifts only the variation in the density-gradient scale length below 1 km has an effect on the unified instability growth rate. Therefore, we expect to see no difference for all practical values of the background values of L_n in the ionosphere during the daytime and nighttime.

Although the linear results show the roles that the density-gradient scale length and cross-field drift play in driving the dominant instabilities in the equatorial electrojet, these results do not show the saturation level of the electron density and the generation of effective Type I 3 m structures that cannot be generated linearly. Therefore, nonlinear simulations are necessary to determine these characteristics of the equatorial electrojet instabilities.

2.2. Nonlinear Results

Several nonlinear simulation results of the turbulence in the plasma density, perturbed electric field, and flux asymmetries in the unified model were presented by *Hassan et al.* [2015], along with a comparison between the plasma turbulence during the solar maximum and solar minimum conditions. The simulation results showed three phases for the plasma turbulence, the growing phase where the linear terms dominate the plasma dynamics, the transition phase where the nonlinear terms have appreciable amplitude compared to the linear terms, and the saturation phase where the dynamics have reached a statistically steady state balance. These three phases in the simulation can be seen in the different study cases in Figure 3.

A comparison between the maximum perturbed electron density for different density-gradient scale lengths is shown in Figure 3, where we can see that the time of the plasma density evolution in the linearly growing domain of the simulation is faster with shorter density scale lengths. Although they are somewhat different in the linear domain, the difference between the plasma density evolution for the cases of $L_n = 4$ km and 6 km is not big in the saturated state of the simulation. However, a short scale length of 1 km makes a big difference, both in the linear growing mode of the perturbed density and in the saturated state, which shows an increase in the maximum fluctuation of the plasma density of more than 5% compared to the background. The small difference between the $L_n = 4$ and 6 km cases supports the linear results of Figure 2, where the variation in the gradient-density scale length above 2 km has a very small effect on the growth rate for $v_E = 400$ m/s.

For the case of strong electron $\boldsymbol{E} \times \boldsymbol{B}$ drift when $v_E = 425$ m/s, different magnitudes of density-gradient scale length ($L_n = 1$ and 6 km) do not translate into differences in the growing mode of the simulation; however, they match perfectly as expected from Figure 2, where the variation in L_n from (approximately) 1 km gives rise to a negligible variation in the linear growth rate under strong driving conditions of the Farley-Buneman instability. At saturation in the simulation, the difference is very small. On the other hand, an increase of the

$\boldsymbol{E} \times \boldsymbol{B}$ drift of 25 m/s with the same density-gradient scale length causes a significant change in the saturation level of the perturbed electron density, it falling in the range between 10 and 15%.

Therefore, these simulation results show the importance of the density-gradient scale length in driving the plasma gradient-drift instability in the absence of Farley-Buneman instability at small magnitudes of the electron drift speeds (below the ion-acoustic speed). However, in the presence of Type I instability the role of the density gradient is negligible in driving the instability for scale lengths larger than 2 km. Moreover, in the case of strong driving conditions with large cross-field drift, the density gradient of any practical scale from 1 km does not play any role in driving the Farley-Buneman instability. This explains the disappearance of the gradient-drift instability from the radar echoes in the presence of the small structures formed in the presence of Farley-Buneman instability and energy cascading mechanism [*Farley*, 2009].

To conclude, the density-gradient and cross-field drifts are coplayers in driving Type II instability in the absence of Type I instability, but they dominate interchangeably at different ranges of values of L_n and v_E. Above the ion-acoustic speed there is a transition region where both the density-gradient and cross-field drifts play important roles in driving both types of instabilities, but at large values of cross-field drifts ($v_E \gg 400$ m/s) the role of density gradient in driving the instabilities is too small to be considered and the Type I instability dominates and its dynamics are controlled by the electron $\boldsymbol{E} \times \boldsymbol{B}$ drift. The study, described below, of the energy distribution of plasma fluctuations of different scales and the forward and reverse cascade of energy among these structures will shed some light on the generation of short- and long-wavelength irregularities in the equatorial electrojet.

3. Energy Components and Transfer in the Unified Fluid Model

In the linear and nonlinear results of Figures 1–3, we showed the effect of different scale lengths of density gradient and electric-potential gradient on the linear growth rate of the unstable modes and the evolution of the perturbed quantities over the growing, transition, and saturation regions of the nonlinear simulation. This demonstrates that available free energy is injected into the system from the vertical boundaries through constant gradients of the plasma density $\partial_z n_o$ and electric potential $\partial_z \phi_o$, with their importance in driving the instabilities varying depending on their local values in the ionosphere. In contrast, the energy is dissipated out of the system due to the electron and ion viscosities, where their collision frequencies with the background neutral particles act as energy sinks.

Therefore, by identifying and separating out the source, dissipation, and dynamical components of the governing unified fluid model of equations (1)–(3), we are poised to trace energy transfer. To this end we rewrite the unified fluid model in the following fully nonlinear form:

$$\partial_t \delta n = \boldsymbol{\nabla} \cdot (\delta n \boldsymbol{\nabla} \delta \chi) + \boldsymbol{\nabla} \cdot (n_o \boldsymbol{\nabla} \delta \chi) \tag{6}$$

$$\partial_t \nabla^2 \delta \chi = \frac{\Omega_{ci}}{B} \nabla^2 \delta \phi + v_{t_i}^2 \nabla^2 \delta n + \frac{1}{2} \nabla^2 |\boldsymbol{\nabla} \delta \chi|^2 - \nu_{\text{in}} \nabla^2 \delta \chi + \frac{4}{3} \frac{v_{t_i}^2}{\nu_{\text{in}}} \nabla^4 \delta \chi \tag{7}$$

$$\begin{aligned} \partial_t \nabla^2 \delta \phi = & -B \Omega_{\text{ce}} n_o^{-1} \boldsymbol{\nabla} \cdot (\delta n \boldsymbol{\nabla} \delta \chi) - B \Omega_{\text{ce}} n_o^{-1} \boldsymbol{\nabla} \cdot (n_o \boldsymbol{\nabla} \delta \chi) - \Omega_{\text{ce}} [\phi_o, \ln(n_o)] \\ & - \Omega_{\text{ce}} [\delta \phi, \ln(n_o)] - \Omega_{\text{ce}} [\phi_o, \delta n] - \Omega_{\text{ce}} [\delta \phi, \delta n] - \frac{1}{B} [\phi_o, \nabla^2 \delta \phi] - \frac{1}{B} [\delta \phi, \nabla^2 \delta \phi] \\ & + \frac{T_e \nu_{\text{en}}}{e} \nabla^2 \ln(n) + \frac{T_e \nu_{\text{en}}}{e} \boldsymbol{\nabla} \ln(n) \cdot \boldsymbol{\nabla} \ln(n) - \nu_{\text{en}} \nabla^2 \phi - \nu_{\text{en}} \boldsymbol{\nabla} \ln(n) \cdot \boldsymbol{\nabla} \phi. \end{aligned} \tag{8}$$

The physics of the ionosphere plasma in the *E* region is such that the energy in the system is contained in the kinetic energy of the magnetized electrons due to the $\delta \boldsymbol{E} \times \boldsymbol{B}$ drifts, the kinetic energy of the unmagnetized ions, and the internal thermal energy in the plasma species. Therefore, the total energy of these three components, respectively, can be written in the following form:

$$E_T = \int \mathrm{d}^2 x' \left(\frac{n_o m_e}{2B^2} |\boldsymbol{\nabla} \delta \phi|^2 + \frac{m_i}{2} \delta n |\boldsymbol{\nabla} \delta \chi|^2 + \frac{1}{2} m_i v_{t_i}^2 \delta n^2 \right), \tag{9}$$

where m_i and m_e are the ions and electrons mass, respectively. The total energy in equation (9) is shown in *Hassan* [2016] to serve as the Hamiltonian of a noncanonical Hamiltonian system [*Morrison*, 1998].

This total energy reaches a saturated state, i.e., when there is zero time-averaged rate of change because of a balance between the energy sources at the system boundaries and the energy sink represented by the electron and ion viscosities, which as noted model their corresponding collisions with the background neutrals. The rate of change of the total energy can be written in terms of the energy source (S), the energy dissipation (D), the nonlinear energy transfer between different scales of plasma structures (N), and the energy coupling between the evolving fields in the system (C) as follows:

$$\begin{aligned}\dot{E}_T &= S + D + N + C \\ &= \{S + D + N + C\}_n + \{S + D + N + C\}_\chi + \{S + D + N + C\}_\phi,\end{aligned} \tag{10}$$

where in the second equality the subscripts represent the contributions from each of equations (6)–(8), respectively. To study the physics in the source, sink, nonlinear, and coupling terms of the three evolving fields (δn, $\delta\phi$, and $\delta\chi$) in equation (9), we need to find the rate of change of the total energy (9), which can be found from the following:

$$\dot{E} = \int \mathrm{d}^2x' \left(-\frac{m_e n_o}{B^2}\delta\phi\partial_t\nabla^2\phi + \frac{m_i}{2}|\boldsymbol{\nabla}\chi|^2\partial_t\delta n - m_i\partial_t\delta\chi\boldsymbol{\nabla}\cdot(n\boldsymbol{\nabla}\delta\chi) + m_i v_{t_i}^2\delta n\partial_t\delta n \right), \tag{11}$$

where we used integration by parts,

$$\int \mathrm{d}^2x'\boldsymbol{\nabla}f\cdot\partial_t\boldsymbol{\nabla}g = \int \mathrm{d}^2x'\boldsymbol{\nabla}\cdot\left(f\partial_t\boldsymbol{\nabla}g\right) - \int \mathrm{d}^2x' f\partial_t\nabla^2 g = -\int \mathrm{d}^2x' f\partial_t\nabla^2 g,$$

in the first and second terms of the integral, which requires either Dirichlet or periodic boundary conditions for all integrated evolving fields represented by f and g, and the periodic boundary condition is employed in the simulation of the dynamical equations in the unified fluid model.

Then, from the set of partial differential equations (6)–(8) that governs the plasma dynamics in the equatorial electrojet instabilities with the energy balance of equation (11), we can rewrite the rate of energy change of the system in the following form:

$$\begin{aligned}\dot{E}_T = \int \mathrm{d}^2x' \Big(& e\delta\phi\left(\boldsymbol{\nabla}\cdot(n_o\boldsymbol{\nabla}\delta\chi) + \boldsymbol{\nabla}\cdot(\delta n\boldsymbol{\nabla}\delta\chi)\right) \\ & + \frac{en_o}{B}\delta\phi[\delta\phi, \ln(n_o)] + [\phi_o, \delta\tilde{n}] + [\delta\phi, \delta\tilde{n}] \\ & + \frac{en_o}{B^2\Omega_{\mathrm{ce}}}\delta\phi\left([\phi_o, \nabla^2\delta\phi] + [\delta\phi, \nabla^2\delta\phi]\right) \\ & - en_o\rho_e^2\nu_{\mathrm{en}}\delta\phi\left(\nabla^2\delta\tilde{n} + 2\boldsymbol{\nabla}\ln(n_o)\cdot\boldsymbol{\nabla}\delta\tilde{n} + \boldsymbol{\nabla}\delta\tilde{n}\cdot\boldsymbol{\nabla}\delta\tilde{n}\right) \\ & + \frac{en_o\nu_{\mathrm{en}}}{B\Omega_{\mathrm{ce}}}\delta\phi\left(\nabla^2\delta\phi + \boldsymbol{\nabla}\ln(n_o)\cdot\boldsymbol{\nabla}\delta\phi + \boldsymbol{\nabla}\delta\tilde{n}\cdot\boldsymbol{\nabla}\phi_o + \boldsymbol{\nabla}\delta\tilde{n}\cdot\boldsymbol{\nabla}\delta\phi\right) \\ & + m_i\nu_{\mathrm{in}}\delta\chi\left(\boldsymbol{\nabla}\cdot(n_o\boldsymbol{\nabla}\delta\chi) + \boldsymbol{\nabla}\cdot(\delta n\boldsymbol{\nabla}\delta\chi)\right) \\ & - \frac{4}{3}\frac{m_i v_{t_i}^2}{\nu_{\mathrm{in}}}\nabla^2\delta\chi\left(\boldsymbol{\nabla}\cdot(n_o\boldsymbol{\nabla}\delta\chi) + \boldsymbol{\nabla}\cdot(\delta n\boldsymbol{\nabla}\delta\chi)\right) \\ & - \left(e\delta\phi + m_i v_{t_i}^2\delta n\right)\left(\boldsymbol{\nabla}\cdot(n_o\boldsymbol{\nabla}\delta\chi) + \boldsymbol{\nabla}\cdot(\delta n\boldsymbol{\nabla}\delta\chi)\right) \\ & + m_i v_{t_i}^2\delta n\left(\boldsymbol{\nabla}\cdot(n_o\boldsymbol{\nabla}\delta\chi) + \boldsymbol{\nabla}\cdot(\delta n\boldsymbol{\nabla}\delta\chi)\right)\Big).\end{aligned} \tag{12}$$

where ρ_e is the electrons gyroradius.

A close look at the physics in equation (12) leads to the understanding of the contribution of each term to the rate of change of the total energy of (9), thereby allowing us to identify the special roles of each in the system dynamics. In this way we identify terms as source (S), dissipation (D), energy transfer (N) of each evolving field,

and energy coupling (C) between the evolving fields. Therefore, we can write their contributions explicitly as follows:

$$
\begin{aligned}
S_\phi &= \int \mathrm{d}^2x' \, \frac{en_o}{B}\delta\phi \left([\delta\phi, \ln(n_o)] + [\phi_o, \delta n] + \frac{1}{B\Omega_{\mathrm{ce}}}[\phi_o, \nabla^2\delta\phi] \right) \\
D_\phi &= \int \mathrm{d}^2x' \, \left(\frac{\mathrm{e}n_o\nu_{\mathrm{en}}}{B\Omega_{\mathrm{ce}}}\delta\phi \left(\nabla^2\delta\phi + \boldsymbol{\nabla}\ln(n_o)\cdot\boldsymbol{\nabla}\delta\phi + \boldsymbol{\nabla}\delta n\cdot\boldsymbol{\nabla}\phi_o + \boldsymbol{\nabla}\delta n\cdot\boldsymbol{\nabla}\delta\phi \right) \right. \\
&\quad \left. - en_o\rho_e^2\nu_{\mathrm{en}}\delta\phi \left(\nabla^2\delta n + 2\boldsymbol{\nabla}\ln(n_o)\cdot\boldsymbol{\nabla}\delta n + \boldsymbol{\nabla}\delta n\cdot\boldsymbol{\nabla}\delta n \right) \right) \\
N_\phi &= \int d^2x' \, \frac{en_o}{B}\delta\phi \left([\delta\phi, \delta n] + \frac{1}{B\Omega_{ce}}[\delta\phi, \nabla^2\delta\phi] \right) \\
C_{\phi\chi} &= \int \mathrm{d}^2x' \, e\delta\phi \left(\boldsymbol{\nabla}\cdot(n_o\boldsymbol{\nabla}\delta\chi) + \boldsymbol{\nabla}\cdot(\delta n\boldsymbol{\nabla}\delta\chi) \right) \\
D_\chi &= \int \mathrm{d}^2x' \left(m_i\nu_{\mathrm{in}}\delta\chi \left(\boldsymbol{\nabla}\cdot(n_o\boldsymbol{\nabla}\delta\chi) + \boldsymbol{\nabla}\cdot(\delta n\boldsymbol{\nabla}\delta\chi) \right) - \frac{4}{3}\frac{m_i\upsilon_{t_i}^2}{\nu_{\mathrm{in}}}\nabla^2\delta\chi \left(\boldsymbol{\nabla}\cdot(n_o\boldsymbol{\nabla}\delta\chi) + \boldsymbol{\nabla}\cdot(\delta n\boldsymbol{\nabla}\delta\chi) \right) \right) \\
C_{\chi\phi} &= -\int \mathrm{d}^2x' \, e\delta\phi \left(\boldsymbol{\nabla}\cdot(n_o\boldsymbol{\nabla}\delta\chi) + \boldsymbol{\nabla}\cdot(\delta n\boldsymbol{\nabla}\delta\chi) \right) \\
C_{\chi n} &= -\int \mathrm{d}^2x' \, m_i\upsilon_{t_i}^2\delta n \left(\boldsymbol{\nabla}\cdot(n_o\boldsymbol{\nabla}\delta\chi) + \boldsymbol{\nabla}\cdot(\delta n\boldsymbol{\nabla}\delta\chi) \right) \\
C_{n\chi} &= \int \mathrm{d}^2x' \, m_i\upsilon_{t_i}^2\delta n \left(\boldsymbol{\nabla}\cdot(n_o\boldsymbol{\nabla}\delta\chi) + \boldsymbol{\nabla}\cdot(\delta n\boldsymbol{\nabla}\delta\chi) \right).
\end{aligned}
\tag{13}
$$

Thus, energy is always injected into the system from the dynamics of the electric potential, S_ϕ, and there is no other energy source that can be recognized in the dynamics of the ion velocity potential or plasma density evolving fields. Part of the energy injected into the system is dissipated internally via the electron viscosity, D_ϕ; however, the other part is transferred to the ions velocity potential dynamical equation through the coupling term, $C_{\phi\chi}$, between the fluctuating electric potential and velocity potential fields that will be dissipated in the collision process of the ions with the background neutral particles, D_χ — more discussion will be provided in section 3.2 where the physical mechanisms of injecting and dissipating energy for the system are discussed.

From the coupling terms in equation (13), we can see that the third term in equation (11) plays the coupling role between the ion velocity potential and the other evolving fields (it also couples with itself). This happens because this term represents conservation in the plasma density in addition to the quasineutrality assumption that is employed in the system. Surprisingly, the dynamics of the ion velocity potential and density are coupled together through a coupling term, $C_{n\chi}$, which is the only term in the continuity equation of the plasma density. This explains the tying of the total energy in the ion velocity potential with the plasma density that is found in Figure 4 and bears on the growing and transitional regimes of the simulations. It is also noticed that there is no direct coupling between the perturbed plasma density δn and the perturbed electric potential $\delta\phi$, and all the coupling dynamics between these two fields has to happen through the cross coupling of these evolving fields and the perturbed ion velocity potential $\delta\chi$.

3.1. Tracking the Total Energy in Simulations

As noted before, the total energy of (9) is composed of three types, the kinetic energy of ions and electrons and the internal thermal energy of the plasma species. The total energy E_T and the ratio between each of the three energy components and the total energy are shown in Figure 4 for the case where $L_n = 6$ km and $\upsilon_E = 400$ m/s. Although it strongly controls the system dynamics through the temporal variations of the electric potential, the electron kinetic energy E_ϕ due to the $\boldsymbol{\delta E}\times\boldsymbol{B}$ drifts makes a very small contribution to the total energy because it depends on the small-amplitude fluctuation of the perturbed electric potential and the small inertia of the electrons. On the other hand, the kinetic energy content of the heavy ions E_χ, depending on both the density and ion velocity potential, has almost double the internal thermal energy E_n in the system. The sum of E_χ and E_n amounts to approximately 98% of the total energy in the dynamical system, as shown in Figure 4 (top).

The ratio between the energy in the evolving fields and the total energy in the system is shown in Figure 4 (bottom). This ratio shows that the plasma internal thermal energy and ion kinetic energy are partially exchanging energy over the growing and transition phases of the simulation. Then, their energy content becomes and remains almost flat during the saturation state. The coupling between the energy components in the ions shown in equation (13) explains the strong tying of the dynamics in the plasma density and ion

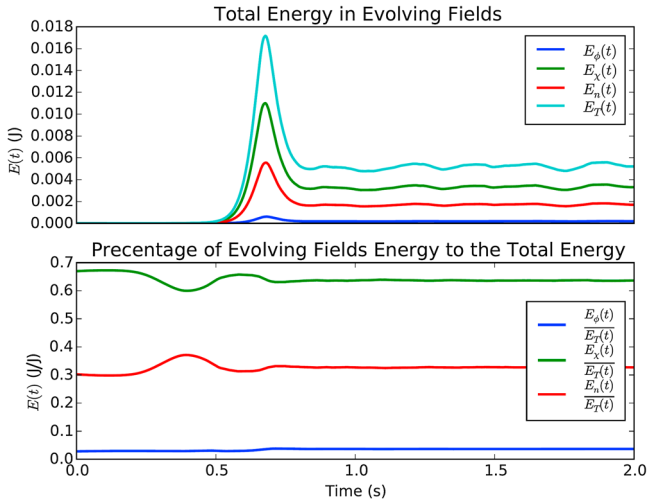

Figure 4. (top) The total energy in the evolving fields ($\delta n, \delta\phi, \delta\chi$) and (bottom) the ratio of the energy in each evolving field to the total energy for $L_n = 6$ km and $v_E = 400$ m/s. This ratio shows the dynamics of the heavy ions that play an important role in evolving the turbulence in the plasma fluid as it contains the largest portion of energy in dynamical system compared to other fields.

velocity potential. The interrelation between the energy content in the plasma density, ion velocity potential, and electron potential has been calculated in other cases with different density-gradient scale-length L_n and cross-field drifts v_E: the energy content of the ion velocity potential is always larger than that of the plasma density, and the perturbed electric potential has the smallest energy content in the system.

A comparison between the total energy profiles for different magnitudes of the plasma density scale length ($L_n = 1, 4, 6$, and ∞ km) and the cross-field drifts ($v_E = 400$ and 425 m/s) is shown in Figure 5. For an electron drift of magnitude $v_E = 400$ m/s, the increase in the density scale length gives rise to an increase of the rate of evolution of the energy in the growing and transition states of the simulation and a different level of the total energy at the saturation region. However, for $v_E = 425$ m/s, the effect of the density scale length is negligible over all phases of energy evolution in the system. The saturation energies in the cases of $L_n = 4, 6$, and ∞ km are almost the same, but it takes more time to reach almost the same level of saturation as the density-gradient scale length increases. The energy at the saturated state of the simulation almost doubles from ~7 mJ when $L_n = 4, 6$, and ∞ km to ~14 mJ when $L_n = 1$ km. Similarly, the energy level almost doubles when the $\boldsymbol{E} \times \boldsymbol{B}$ drift increases from $v_E = 400$ m/s to $v_E = 425$ m/s.

These results underscore the fact that the density scale-length L_n and the cross-fields drift v_E are the energy sources in our dynamical system and that they play important roles in driving the system in its linear growing mode phase and ultimate termination at different saturation levels. While a small increase in the cross-field drift (from $v_E = 400$ m/s to $v_E = 425$ m/s) causes a dramatic increase in the growth rate of the unstable modes and results in a larger amplitude of the fluctuating density, changes in the density-gradient scale length do not show the same effect, especially for the cases of $L_n = 4, 6$, and ∞ km. However, when the scale length of the density gradient ($L_n = 1$ km) approaches the effective size of the simulation box ($L_z = 0.1$ km), we noticed a large change in the growth rate of the unstable modes and the maximum perturbed density, but one that is still not comparable to the change induced by the cross-field drifts v_E. Therefore, these results again show that the effect of different combinations of the density-gradient scale-length L_n and cross-field drift speed v_E on driving the instabilities in the system is similar to the linear and nonlinear results described in sections 2.1 and 2.2.

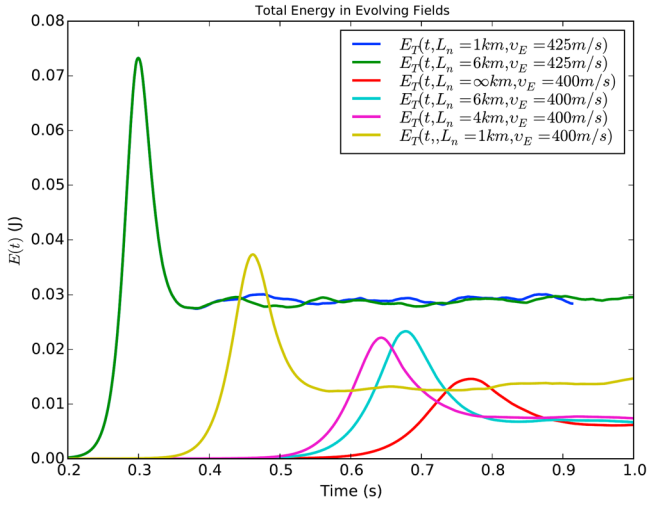

Figure 5. A comparison between the total energy (the sum of the ion and electron kinetic energy and the plasma internal energy) for different magnitudes of the density scale-length $L_n = 1, 4, 6$, and ∞ (km) and drifts $v_E = 400$ and 425 (m/s).

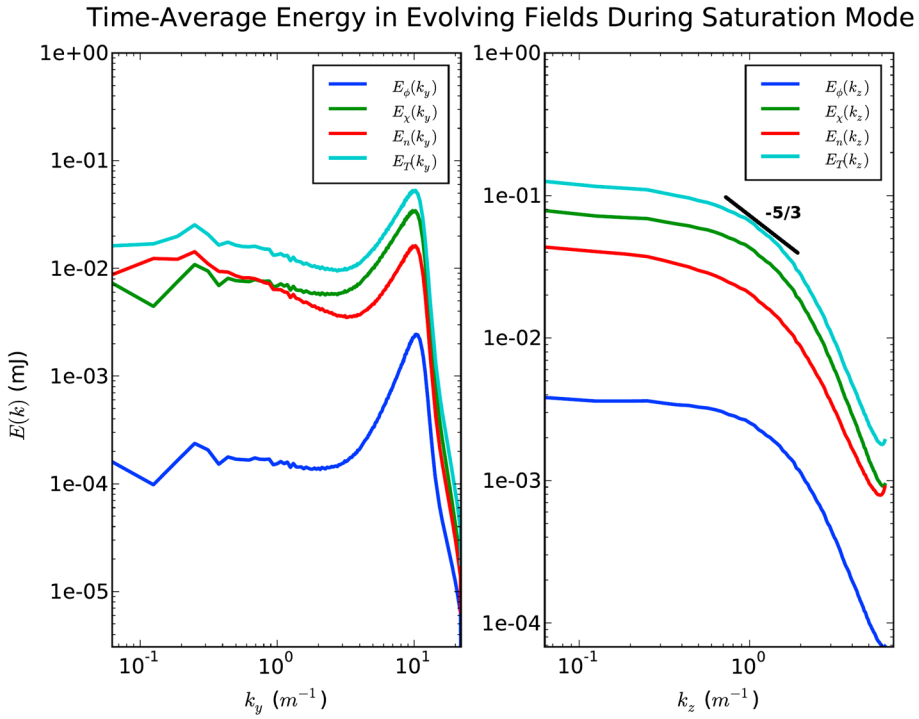

Figure 6. The time average of the energy in the evolving fields $(\delta n, \delta\phi, \delta\chi)$ and their corresponding total energy during the saturation state of the simulation for $L_n = 6$ km and $v_E = 400$ m/s as a function of the (left) horizontal (k_y) and (right) vertical (k_z) wave numbers.

The time average of the total energy and its components as a function of the horizontal wave number k_y and vertical wave number k_z during the saturated state of the simulation is shown in Figure 6, for $L_n = 6$ km and $v_E = 400$ m/s. The two peaks at small and large wave numbers that were seen in the linear growth rate versus k_y are still found during the nonlinear saturated state as shown in Figure 6 (left). The peak at the small wave number is still around 0.1 m^{-1}, similar to the corresponding peak in the linear growth rate. However, the peak at the large wave number has shifted from ~7–8 m^{-1} to ~10–11 m^{-1}. This suggests that the nonlinear dynamics of the system transfers energy to structures of smaller wavelength, which would explain the strong backscattering of radar echoes that come from the short structures compared to long ones and the disappearance of the Type II instability in the presence of Type I instability, and agrees with the large growth rate of small-scale structures compared to the growth rate of the unstable waves of long wavelength in the linear regime. It is also found that the size of the small plasma structures that have the largest energy content is strongly dependent on the magnitudes of the density-gradient scale-length L_n and cross-field drifts (v_E).

The time average of the energy in the vertical direction of k space during the saturation mode is shown in Figure 6 (right). The amount of energy content in the small structures is 1 order of magnitude larger than the amount of energy content in the corresponding structures in the horizontal direction. According to this scale-dependent energy content, one would expect to observe strong echoes from the vertical structures of 1–5 m scale size and not from the horizontal ones of the same scale, which is consistent with the recorded radar observations [*Kudeki et al.*, 1987] and sounding rocket measurements [*Pfaff et al.*, 1987a, 1987b] during the CONDOR campaign. Moreover, while no explicit power law can be found in the horizontal and vertical k space, these results also suggest the presence of a forward energy cascading mechanism to transfer the energy from large plasma structures into small ones, which will be discussed further in section 4.

3.2. Energy Sources and Dissipations

Although studying the rate of energy transfer in each of the evolving fields $(\delta n, \delta\phi, \delta\chi)$ in equation (11) verifies total energy conservation of the system, it does not show the role each field plays as source, sink, cross-field coupling, or inner field coupling, and the various redistribution mechanisms of components of the total energy.

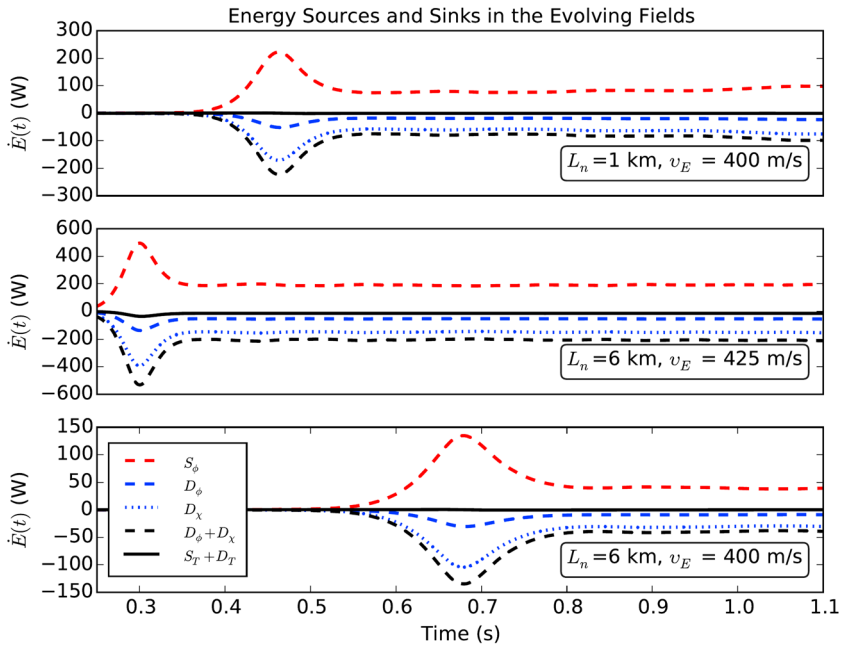

Figure 7. The total rate of change of energy sources and sinks for the evolving fields over the transition and saturation phases of the simulation for the cases $L_n = 1$ and 6 km and $v_E = 400$ and 425 m/s. This shows the dependence of the beginning of the transition and saturation regions of the simulation on the magnitude of the energy sources (L_n and v_E).

In Figure 7 we show the various sources and dissipation of the energy in the ions and electrons for different magnitudes of the density-gradient scale length ($L_n = 1$ and 6 km) and cross-field drift ($v_E = 400$ and 425 m/s). In all cases of the simulation, the major source of energy input for the unified fluid mode is the electron kinetic energy, which also dissipates a small part of that energy via collisions of the electrons with neutrals. However, the heavy ions are responsible for most of the dissipation of energy in the system because of their large collision frequency with the neutral particles in the atmosphere. In our representation of energy sources and dissipation, we do not include the coupling terms between the evolving fields because they cancel each other, as can be shown from equation (12).

In all the cases of Figure 7, we found that the total dissipation in the ions and electrons due to collisions is equal to the total energy coming into the electron dynamics from the sources, the gradients of the background density, and electric potential in the vertical direction. So we have determined that the entire system satisfies energy conservation between the three evolving fields, as represented by the black solid line that passes through the x axis at $\dot{E}_T = 0$.

Two more examples for the magnitudes of the energy sources and dissipation for different values of density scale length ($L_n = 6$ km) and cross-field drift speed ($v_E = 425$ and 400 m/s) are shown in Figure 7 (middle and bottom). A comparison between the results in the three panels elucidates the significant effect of any small change in the $\boldsymbol{E} \times \boldsymbol{B}$ drifts on the evolution of the equatorial electrojet instabilities. This is due to the availability of a large amount of free energy in the system. A similar but smaller effect takes place with a short density-gradient scale length ($L_n = 6$ km versus $L_n = 1$ km). This means that our system drives the Farley-Buneman (Type I) instability stronger than the gradient-drift (Type II) instability when the cross-field drift is much larger than the magnitude of the ion-acoustic speed in the local ionosphere.

We further investigated the behavior of each term in the energy equation in conserving the energy in the system. We included only the terms that add, couple, or dissipate appreciable amounts of energy, dropping very small terms that are at least 3 orders of magnitude smaller than those kept.

Figure 8 shows that the major source of energy (S_ϕ) comes from

$$S_\phi = \int \mathrm{d}^2x\, n_e T_e v_E\, \delta\tilde{\phi}\, \partial_y \delta\tilde{n},$$

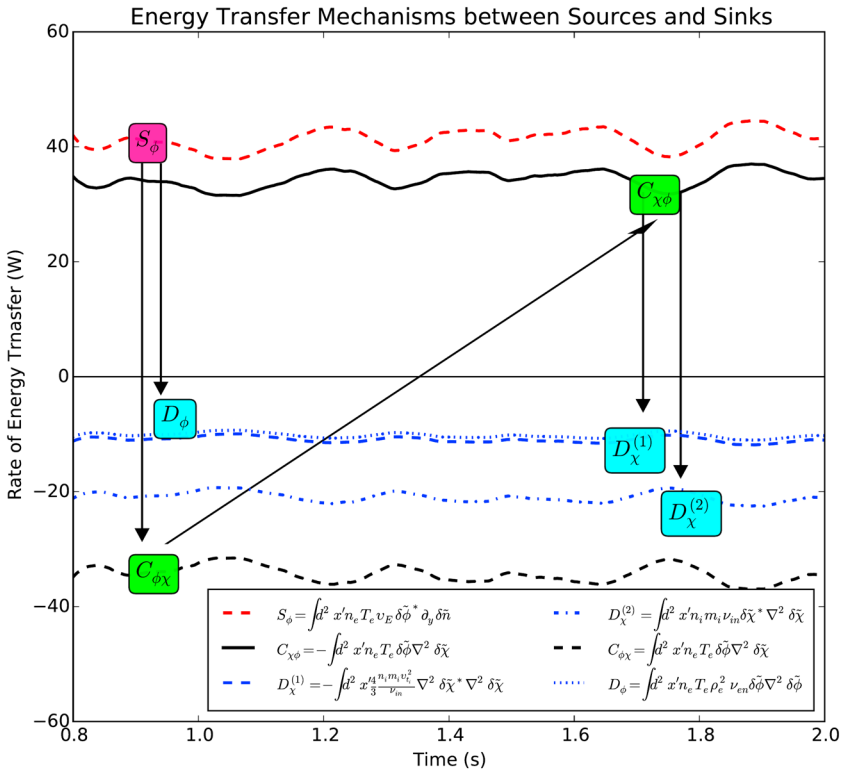

Figure 8. The energy transfer mechanism and physics between the source and sink terms over the saturation state of the simulation for a case of $L_n = 6$ km and $v_E = 400$ m/s and the coupling between the fields. The thermal internal energy in the density field is not shown here because it is only coupled with the ion velocity potential and it has a very small magnitude.

which adds about 40 J every second to the system. This term plays the role of the electron cross-field drift velocity along with the gradient of the fluctuating density in the horizontal direction in driving the two-stream instability, where the secondary electric field and density gradient are antiparallel to each other causing the growth of the unstable modes.

Due to collisions of electrons with the background, 10 J are dissipated every second in the diffusion of the fluctuating electric field (D_ϕ),

$$D_\phi = \int \mathrm{d}^2x\, n_e T_e \rho_e^2 \nu_{\mathrm{en}}\, \delta\tilde{\phi}\, \nabla^2 \delta\tilde{\phi};$$

however, the rest of the energy injected into the system is absorbed into the plasma internal energy via coupling between the dynamics of the electrons and ions.

The energy that is transferred to the ion dynamical equation as it couples with the electric potential dynamics ($C_{\phi\chi}$) through,

$$C_{\phi\chi} = \int d^2x\, n_e T_e\, \delta\tilde{\phi} \nabla^2 \delta\tilde{\chi}$$

dissipates via the ion collisional and viscosity terms ($D_\chi^{(1)}$ and $D_\chi^{(2)}$) through

$$D_\chi^{(1)} = -\int \mathrm{d}^2x\, \frac{4}{3} \frac{n_i T_i}{\nu_{\mathrm{in}}} \nabla^2 \delta\tilde{\chi} \nabla^2 \delta\tilde{\chi}, \quad \text{and} \quad D_\chi^{(2)} = \int \mathrm{d}^2x\, n_i m_i \nu_{\mathrm{in}}\, \delta\tilde{\chi} \nabla^2 \delta\tilde{\chi}$$

respectively. It was found that the dissipation in the collisional part is almost double that due to viscosity, which explains the importance of the ion collisions with the background compared to the ion viscosity in stabilizing the unstable modes and saturating the evolving fields.

To conclude, the electron dynamics injects energy into the system and the major source of energy comes from the cross-field drift when it exceeds the ion-acoustic speed. The injection of the energy through the density gradient is small for the current simulation conditions compared to the other source of energy. The collisions of the ions and electrons with neutrals provide a large sink for the available energy in the dynamical system. In addition, the ion viscosity dissipates one third of the transferred energy to the ion nonlinear dynamics, which is also a stabilizing factor in the linear regime. The coupling between the dynamics of the ions and electrons takes place through the diffusion of the species.

4. Small-Scale Structures and Energy Cascading

In section 3 we identified three kinds of energy: sources that inject energy into the system, sinks that suck energy out of the system, and (nonlinear) transfer terms that redistribute energy between structures of different scale sizes in the system. The transfer terms are responsible for the generation of plasma irregularities that cannot be generated linearly. In equation (13) we identified two nonlinear terms, N_ϕ, whose sum over k space should vanish at each time step, yet they are responsible for transferring energy between the stable/unstable modes. These two transfer terms come from the equation for the perturbed electric potential, which elucidates the role of the electron dynamics in cascading energy between the modes at different wave numbers and, thereby, generating multiscale plasma structures.

The first transfer term ($N_\phi^{(1)}$), which is defined as

$$N_\phi^{(1)} = \int \mathrm{d}^2x \, \frac{en_o}{B} \, \delta\tilde{\phi}[\delta\tilde{\phi}, \delta\tilde{n}] \tag{14}$$

is shown during the saturation stage of the simulation in Figure 9 (left column) for $L_n = 6$ km and $v_E = 400$ m/s. The color contour plot in Figure 9 (top row) shows this term integrated in the vertical direction as a function of time and the horizontal wave number (k_y), where we can see a steady transfer of energy between the unstable modes over the saturation phase without much variation in time. Figure 9 (bottom row) shows the time average of the energy content of $N_\phi^{(1)}$ of (14) as a function of k_y. From these panels we can see a forward energy cascade, where the rate of energy change is negative in the region of small wave number $k_y \leq 5.0\ \mathrm{m}^{-1}$ (red) and positive in the region above $k_y \geq 5.0\ \mathrm{m}^{-1}$ (blue).

This indicates that the Poisson bracket $[\delta\tilde{\phi}, \delta\tilde{n}]$ transfers energy from long structures of small wave number to the small structures of large wave number. The energy is transferred in successive cascading processes to smaller structures until it ends at structures of a meter or less with a peak in the range of $k_y = 9.0\text{–}11.0\ \mathrm{m}^{-1}$. Above $k_y = 15\ \mathrm{m}^{-1}$, the energy content is almost zero. These results are in agreement with the radar observations that suggest that submeter structures with very small energy content scatter the radio frequency signals, while all structures above half a meter are expected to be seen in the radar echoes when the proper frequency is used.

The other nonlinear term is responsible for energy cascading, as shown in Figure 9 (right column). However, the effect of the second transfer term ($N_\phi^{(2)}$), which is defined as

$$N_\phi^{(2)} = \int \mathrm{d}^2x \, \frac{en_o}{B} \, \delta\tilde{\phi}[\delta\tilde{\phi}, \nabla^2\delta\tilde{\phi}], \tag{15}$$

is much smaller than $N_\phi^{(1)}$ due to the small amount of cascading energy (note the *milliwatts* (Figure 9, bottom left) and *microwatts* (Figure 9, bottom right) units on the y axis). The Poisson bracket $[\delta\tilde{\phi}, \nabla^2\delta\tilde{\phi}]$ shows two overlapped regions of forward and inverse energy cascading. The first region again at $k_y = 0.0\text{–}5.0\ \mathrm{m}^{-1}$, where the energy is transferred via a forward cascade from a very narrow region of long-scale structures around the size of the simulation box at $k_y \sim 0.1\ \mathrm{m}^{-1}$ to the smaller structures of order of $\lambda \simeq 1\text{–}10$ m. In the second region at $k_y = 1\text{–}15\ \mathrm{m}^{-1}$, we can see dual energy cascading mechanisms. In the right half of the second region ($k_y \leq 4\pi$) the energy is inversely cascaded from short structures of $\lambda \simeq 0.75\text{–}1.00$ m to the longer structures of order $\lambda \simeq 1\text{–}10$ m. This underscores the fact that the Farley-Buneman instability itself can generate structures of long wavelength as proposed by *Kudeki et al.* [1987] in the top part of the *E* region that has a negative density scale length. But this possibility here is limited by the smallness of the amount of energy inversely cascaded to large-scale plasma structures. On the other half of the second region we can see a forward energy cascade to irregularities of scale length less than half a meter. Upon checking the peaks and the spectral spread in the two halves of the second region, we can see that the effect of the forward cascading in the second region is

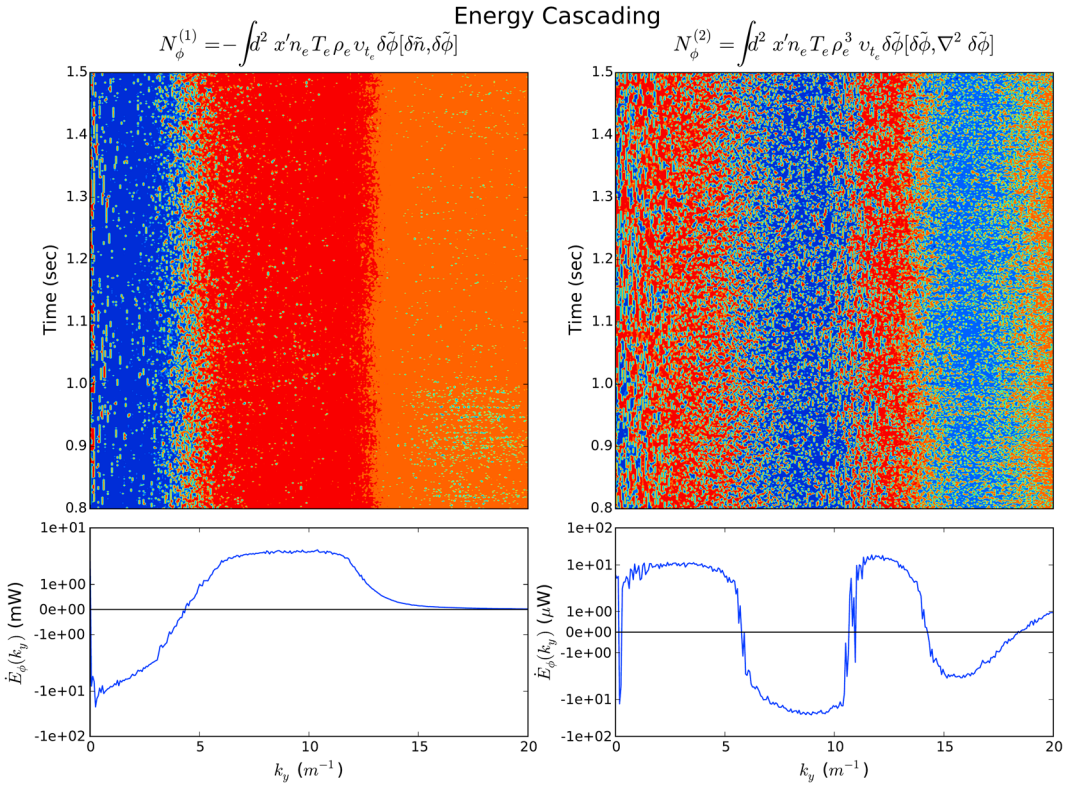

Figure 9. Forward and dual energy cascades over the saturation state of the simulation for a case of $L_n = 6$ km and $v_E = 400$ m/s. (top row) The rate of energy transfer over the saturation time as a function of the (left column) horizontal (k_y) and (right column) vertical (k_z) wave numbers. (bottom row) The average rate of energy transfer over the entire saturation regime as a function of k_y and k_z. Figure 9 (bottom left) shows the role of $N_\phi^{(1)}$ in transferring the energy from the large structures to the small ones; however, the $N_\phi^{(2)}$ is responsible of transferring the energy in forward and reverse directions over different regions of wave numbers but with smaller effect compared to $N_\phi^{(1)}$.

stronger than that of the reverse cascading that has a smaller peak and gets energy from the two regions in independent energy cascading processes.

To ensure that the forward inverse energy cascades are the major factors in generating the small and large plasma irregularities, respectively, in the equatorial electrojet, we made a comparison in Figure 10 between the energy cascading terms and the free energy (the sum of energy sources and dissipations) available in the system dynamics in the horizontal (k_y) and vertical (k_z) directions. It can be seen in Figure 10 that the sources and sinks largely cancel, leaving the nonlinear transfer terms to redistribute the energy into a state where a balance can occur. This emphasizes the role of the nonlinear terms in generating the unstable plasma waves of small wavelength in the equatorial electrojet when there is no source of free energy available in the domain of small structures to be responsible for generating them.

A similar comparison between the role of $N_\phi^{(1)}$ and $N_\phi^{(2)}$ in cascading the energy between the unstable modes of different scales in the vertical direction is seen in Figure 10 (bottom). Both nonlinear terms are responsible for generating small structures through the forward energy cascading mechanism (red and blue solid lines), where there are no linearly unstable modes available that can explain the generation of these structures. These forward energy cascades transfer the energy content in the plasma waves of long structures to structures of wavelength 1–5 m. These are the effective wavelength seen in the backscattering spectral echoes of the radar observations. This is further evidence for the two-step theory of *Sudan et al.* [1973]; i.e., energy cascading gives rise to the nonlinear generation of plasma structures of 3 m length observed in the equatorial electrojet, which cannot be explained by linear theory.

It can also be noticed in Figure 10 that there is a positive rate of energy transfer around $k_y = 4$ m^{-1} (top) and a negative rate of energy transfer around $k_z = 1$ m^{-1} (bottom). Although this imbalance in the rate of energy

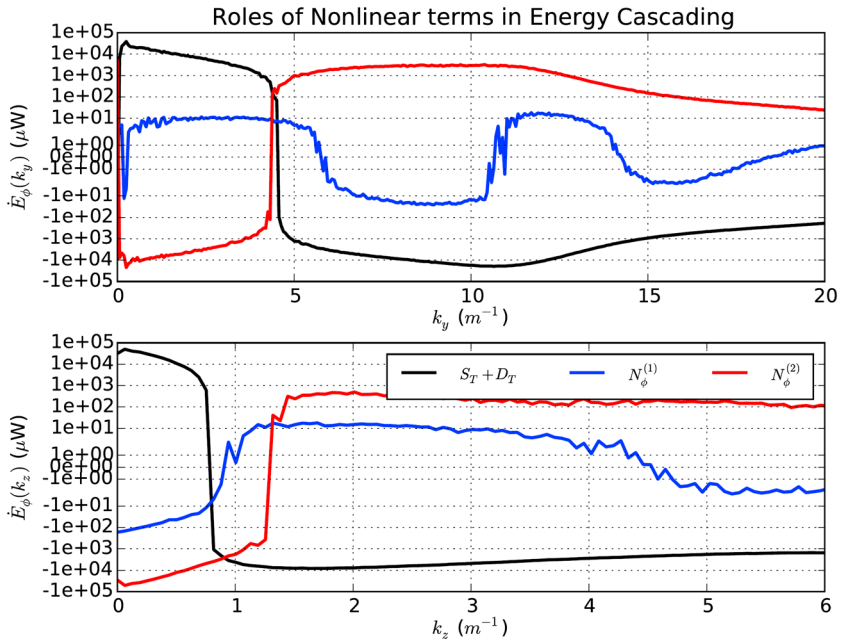

Figure 10. A comparison between the rate of energy transfer in the two nonlinear terms and the sum of the source and sink terms of energies over the saturation state of the simulation for a case of L_n = 6 km and v_E = 400 m/s. This emphasizes on the responsibility of the nonlinear energy transitional terms ($N_\phi^{(1)}$ and $N_\phi^{(2)}$) in generating the small structures in the dynamical system which cannot be generated linearly due to the absence of energy sources at these wave numbers.

transfer is 6 orders of magnitude less than the average rate of energy transfer in the system, it can cause an increase of energy over time. However, this imbalance in energy transfer between the unstable active modes in the dynamical system is due to the small time window we have for calculating the energy due to the large cost of computation. But a larger time window will show a large-scale wave of the perturbed electron density (in the saturation regime) with the small-scale fluctuations superimposed on the top, which may give rise to

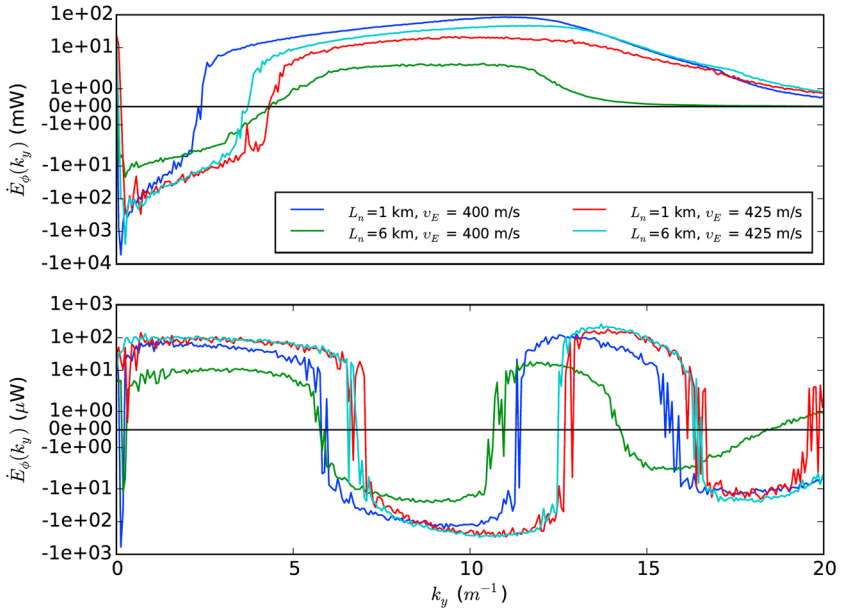

Figure 11. A comparison between the forward and reverse energy cascades over the saturation state of the simulation for different cases of L_n = 1 and 6 km and v_E = 400 and 425 m/s.

a balance in energy transfer over a properly selected longer period of time. The superimposing of the small fluctuations that are caused by the Farley-Buneman instability on the top of large oscillations caused by the gradient-drift instability is in good agreement with the rocket observations by *Pfaff et al.* [1987b].

An interesting comparison between simulation results for forward and reverse energy cascading mechanisms associated with the unstable modes as they enter the nonlinear regime is shown in Figure 11, for two density scale lengths (L_n = 1 and 6 km) and two electron cross-field drifts (v_E = 400 and 425 m/s). The first interesting point is the similarity of the cascading in Figure 11 for different magnitudes of the density scale length at the same $\delta \boldsymbol{E} \times \boldsymbol{B}$ drift value of v_E = 425 m/s, a similarity that is observed in Figure 11 (top and bottom). While the difference between the rate of energy transfer of the evolving modes in the Poisson bracket $[\delta\tilde{\phi}, \delta\tilde{n}]$ in $N_\phi^{(1)}$ at v_E = 425 m/s is smaller than the difference between the corresponding profiles at v_E = 400 m/s, that difference is negligible in the Poisson bracket $[\delta\tilde{\phi}, \nabla^2\delta\tilde{\phi}]$ in $N_\phi^{(2)}$. It is also surprising to find that the rate of forward energy cascade in Figure 11 (top) is small in the case of the sharp density gradient (i.e., small density scale length) when v_E = 425 m/s, in contrast to the cases where v_E = 400 m/s. This comparison shows that the density-gradient scale length manifests itself in transferring energy from large-scale structures to small-scale ones when the cross-field drift is not too much greater than the ion-acoustic speed where the density-gradient scale length (L_n) does not have a significant effect on the energy cascading.

Thus, the polarization drift of the electrons helps in understanding the generation of structures of order smaller than a meter and in understanding the inverse energy cascade that allows the generation of long-wavelength structures in the absence of the gradient-drift instability conditions in the ionospheric background. These simulation results substantiate the *Sudan et al.* [1973] two-step theory for energy cascading to the small-scale structures, irregularities in the horizontal and vertical directions, of the equatorial electrojet.

5. Summary

In this paper we have analyzed and studied properties of the unified fluid model for equatorial electrojet phenomena of *Hassan et al.* [2015]. Simulations with parameters set to various ionospheric background conditions revealed properties of the gradient-drift and Farley-Buneman instabilities. The effect of the density-gradient scale length on the evolution of the instabilities was examined in both the linear and nonlinear regimes. It was found that the sharper the density gradient (i.e., the shorter the scale-length L_n), the larger the growth rate in the linear regime for the gradient-drift and Farley-Buneman instabilities. It was seen that the density-gradient scale length influences unstable modes of all sizes in the electrojet. In contrast, changes in the cross-field $\boldsymbol{E} \times \boldsymbol{B}$ drift did not have any noticeable effect on plasma structures of long wavelength but did have a strong effect on small-scale plasma structures.

A parameter scan for determining the effects of L_n and v_E on the linear growth rate showed five different regions based on the magnitude of the ion-acoustic speed: two upper regions when the cross-field drift exceeds the ion-acoustic speed and three when the cross-field drift is below this value. Type II plasma instability dominates in the three regions where the cross-field speed is smaller than the ion-acoustic speed and the magnitude of the density-gradient scale length controls the dynamics. However, Type I plasma instability dominates the regions where the cross-field drift is much larger than the ion-acoustic speed, where the density-gradient scale length does not show a large effect. In the transition region, which is characterized by cross-field drifts close to the ion-acoustic speed, both the v_E and L_n play important roles in driving both types of instabilities.

In the nonlinear simulation results, the cross-field drift of 425 m/s injects more energy in the system and the unstable modes grow faster and reach higher values at the saturation phase of the simulation compared to the results with only 400 m/s cross-field drift for the same values of density-gradient scale length. It is also found that the density-gradient scale length has a negligible effect on nonlinear simulation results in the case of 425 m/s drift over all phases of simulation; however, the sharper density-gradient causes a sharp growing of the unstable modes in the linear phase of the simulation at 400 m/s drift.

To better understand the physics of the plasma instabilities, we studied the total energy budget of the unified fluid model, composed of the three components: the kinetic energy of electrons and ions and the internal energy of both species. We observed that the internal energy and the ion kinetic energy are linked together

and contain about 98% of the system energy, while the electron kinetic energy comprises less than 2% of the total energy. The reason for this link between the density and the ion velocity potential was traced to the fact that their dynamical equations are perfectly coupled together.

We also categorized the rate of change of energy into sources, sinks, transfer, and coupling terms, where the sources of the energy entered the system from the boundaries through gradients of the background electron density and electric potential, while energy is dissipated by the viscosity of the electrons and ions as they collide with the background neutrals. As an important verification of the code, we determine that the system conserves energy and has very good balance between energy sources and sinks.

In order to understand the generation of structures of various scales (both horizontal and vertical) in the electrojet, we examined the nonlinear transfer of energy. Forward and reverse dual energy cascading was found in the system in the horizontal direction. The Poisson bracket $[\delta\tilde{\phi}, \delta\tilde{n}]$ was observed to be responsible for a large forward cascade from structures of large wavelength (small wave numbers) to generate plasma waves of short wavelength. The other Poisson bracket $[\delta\tilde{\phi}, \nabla^2\delta\tilde{\phi}]$ was seen to be 3 orders of magnitude less effective than the first. However, it was seen to produce concurrent forward and inverse energy cascading between structures of different scales. This Poisson bracket is responsible for the second step of forward cascading of energy to further smaller structures in the equatorial electrojet and inversely cascading energy that generates plasma waves of large sizes. In the vertical direction, forward energy cascading dominates the dynamics in both nonlinearities and was seen to be responsible for the generation of the 2–5 m structures, which cannot be generated by linear dynamics. Our study of the forward and inverse energy cascading was seen to substantiate the two-step energy cascading theory proposed by *Sudan* [1973].

We presented new achievements in the coupled instabilities in a dynamic system that conserves energy and forms a noncanonical Hamiltonian system. Also, we verified the two-step energy cascading mechanism in the equatorial electrojet region and studied closely the effect of the density-gradient scale lengths and cross-field drifts on the evolution and saturation of the turbulent plasmas. The concentration of the energy available in the system in the small structures agrees with the radar observations that show that the spectrum of the backscattered echoes is dominated by these small wave structures.

Acknowledgments
Hassan, E. would like to thank Ioannis Keramidas Charidakos for valuable feedback and fruitful discussions. Hatch, D.R. and Morrison, P.J. were supported by the U.S. Department of Energy contract DE-FG02-04ER54742. The data in the paper are generated from simulations using a locally developed software.

References

Balsley, B. B. (1969), Some characteristics of non-two-stream irregularities in the equatorial electrojet, in *Low-Frequency Waves and Irregularities in the Ionosphere*, edited by N. D'angelo, pp. 152–172, Springer, Netherlands.

Bowles, K. L., B. B. Balsley, and R. Cohen (1963), Field-aligned *E*-region irregularities identified with acoustic plasma waves, *J. Geophys. Res.*, *68*(9), 2485–2501.

Buneman, O. (1963), Excitation of field-aligned sound waves by electron streams, *Phys. Rev. Lett.*, *10*, 285–287.

Farley, D. T. (1963), A plasma instability resulting in field-aligned irregularities in the ionosphere, *J. Geophys. Res.*, *68*, 6083–6097.

Farley, D. T. (2009), The equatorial *E*-region and its plasma instabilities: A tutorial, *Ann. Geophys.*, *27*(4), 1509–1520.

Farley, D. T., and B. B. Balsley (1973), Instabilities in the equatorial electrojet, *J. Geophys. Res.*, *78*, 227–239.

Fejer, B. G., D. T. Farley, B. B. Balsley, and R. F. Woodman (1975), Vertical structure of the VHF backscattering region in the equatorial electrojet and the gradient drift instability, *J. Geophys. Res.*, *80*, 1313–1324.

Forbes, J. M. (1981), The equatorial electrojet, *Rev. Geophys.*, *19*(3), 469–504.

Hassan, E. (2016), Plasma turbulence in the equatorial electrojet observations, theories, models, and simulations, PhD dissertation, Department of Physics, University of Texas at Austin, Austin, Tex.

Hassan, E., W. Horton, A. Smolyakov, S. Litt, and D. Hatch (2013), Nonlocal unified type-I and type-II model of the low-latitude E-region irregularities at solar minimum and solar maximum, AGU Fall Meeting, San Francisco, Calif., 9–13 Dec.

Hassan, E., W. Horton, A. Smolyakov, and D. Hatch (2014), Equatorial Electrojet Instabilities - New Fluid Model Approach, 56th Annual Meeting of the APS Division of Plasma Physics, New Orleans, La, 27–31 October.

Hassan, E., W. Horton, A. I. Smolyakov, D. R. Hatch, and S. K. Litt (2015), Multiscale equatorial electrojet turbulence: Baseline 2-D model, *J. Geophys. Res. Space Physics*, *120*, 1460–1477, doi:10.1002/2014JA020387.

Hysell, D. L., and J. D. Burcham (2000), Ionospheric electric field estimates from radar observations of the equatorial electrojet, *J. Geophys. Res.*, *105*(A2), 2443–2460.

Hysell, D. L., J. Drexler, E. B. Shume, J. L. Chau, D. E. Scipion, M. Vlasov, R. Cuevas, and C. Heinselman (2007), Combined radar observations of equatorial electrojet irregularities at Jicamarca, *Ann. Geophys.*, *25*, 457–473.

Kelley, M. C. (2009), *The Earth's Ionosphere, Plasma Physics and Electrodynamics*, 2nd ed., Academic Press, Amsterdam, and Boston, Mass.

Kudeki, E., and D. T. Farley (1989), Aspect sensitivity of equatorial electrojet irregularities and theoretical implications, *J. Geophys. Res.*, *94*(A1), 426–434.

Kudeki, E., B. G. Fejer, D. T. Farley, and C. Hanuise (1987), The CONDOR equatorial electrojet campaign: Radar results, *J. Geophys. Res.*, *92*, 13,561–13,577.

Lu, F., D. T. Farley, and W. E. Swartz (2008), Spread in aspect angles of equatorial *E* region irregularities, *J. Geophys. Res.*, *113*, A11309, doi:10.1029/2008JA013018.

Morrison, P. J. (1998), Hamiltonian description of the ideal fluid, *Rev. Mod. Phys.*, *70*(2), 467–521.

Pfaff, R. F., M. C. Kelley, E. Kudeki, B. G. Fejer, and K. Baker (1987a), Electric field and plasma density measurements in the strongly driven daytime equatorial electrojet: 1. The unstable layer and gradient drift waves, *J. Geophys. Res.*, *92*, 13,578–13,596.

Pfaff, R. F., M. C. Kelley, E. Kudeki, B. G. Fejer, and K. D. Baker (1987b), Electric field and plasma density measurements in the strongly driven daytime equatorial electrojet: 2. Two-stream waves, *J. Geophys. Res.*, *92*, 13,597–13,612.

Pfaff, R. F., Jr., M. H. Acua, P. A. Marionni, and N. B. Trivedi (1997), DC polarization electric field, current density, and plasma density measurements in the daytime equatorial electrojet, *Geophys. Res. Lett.*, *24*, 1667–1670.

Schmidt, M. J., and S. P. Gary (1973), Density gradients and the Farley-Buneman instability, *J. Geophys. Res.*, *78*, 8261–8265.

Sudan, R. N., J. Akinrimisi, and D. T. Farley (1973), Generation of small-scale irregularities in the equatorial electrojet, *J. Geophys. Res.*, *78*(1), 240–248.